Synthesis and Characterization of Nanostructured Composites for Lithium Batteries

Xuanyu Cao*

New Campus of Tai'an No.3 High School of Shandong Province, Tai'an 273100, China

*Corresponding author's e-mail: xuanyucao36@163.com

Abstract. Currently, with the rapid development of emerging economies and the increasing energy demands in various countries, global energy consumption is sharply rising. To meet these growing energy needs while avoiding the depletion of global resources and long-term environmental damage, finding high-performance, low-cost, and environmentally friendly energy systems has become an urgent issue. Secondary batteries, particularly secondary lithium-ion batteries, are highly anticipated. Leveraging the advantages of nanotechnology and composite technology, this paper focuses on the synthesis and characterization of nanostructured composite materials for lithium-ion batteries. Different morphologies of $ZnFe_2O_4$ nanomaterials were prepared and combined with graphene, enhancing the conductivity of $ZnFe_2O_4$ anode materials and effectively addressing the agglomeration issues that arise during the cycling process of $ZnFe_2O_4$ electrode materials.

Keywords: Lithium battery; Nanostructure; Composite material; Material synthesis; Material characterization.

1 Introduction

Lithium-ion batteries initially employed metallic lithium as the anode material. This configuration not only enabled support for higher output voltages but also accommodated a broader operating temperature range. However, when lithium comes into contact with liquid electrolytes, a passivation reaction occurs on its surface, forming an insulating layer. This layer impedes ion transport, adversely affecting energy transfer and electrochemical stability.

The modification of lithium metal anodes has long been a research focus in the field of lithium-ion batteries. To enhance the safety performance of lithium-ion batteries, selecting more suitable alternative materials to replace lithium metal anodes is a more ideal solution than alloying with other metals. Compared to elemental lithium, ionic lithium exhibits greater stability. This not only improves the safety performance of rocking chair batteries but also endows them with excellent cycle life. Since the advent of the "rocking chair battery", rechargeable lithium-ion batteries have entered a phase of rapid development, sparking a global research boom in materials for rechargeable lithium-ion batteries[1,2].

J. Rak et al. (eds.), *Proceedings of the 2026 11th International Conference on Social Sciences and Economic Development (ICSSED 2026)*, Advances in Economics, Business and Management Research 391,
https://doi.org/10.2991/978-94-6239-701-9_35

2 Introduction to Lithium-Ion Battery

The electrode material system of lithium batteries consists of both cathode and anode materials, which primarily achieve energy storage and release through their synergistic interaction. The core function of cathode materials lies in providing active sites for lithium-ion insertion/extraction, thus requiring a high redox potential to ensure the battery's output voltage remains within a reasonable range. The design principle for anode materials is to approach the electrochemical potential of metallic lithium as closely as possible, thereby maximizing the battery's energy density. Consequently, common choices for anode materials include carbon-based substances such as carbon black, graphite, and mesophase carbon microspheres, as well as alloys and metal oxides like tin-based alloys and their oxides[3,4].

3 Synthesis Methods and Characterization

3.1 Synthesis Method

Hydrothermal and solvothermal methods primarily achieve material transformation by creating a reaction environment. This high-temperature, high-pressure environment fundamentally alters the physicochemical properties of the solvent. When the internal system reaches a supersaturated state, phase separation occurs between the solute and solvent. Following nucleation, the pressure field accelerates the transport of solvent molecules and ions to the crystal interface. These molecules adsorb onto the surface, promoting continuous crystal growth along specific crystal planes.

In this study, $ZnFe_2O_4$ nanomaterials and $ZnFe_2O_4$/graphene composites were prepared using hydrothermal and solvothermal methods. The reaction setup is shown in Figure 1, consisting of an aluminum outer shell and a polytetrafluoroethylene inner liner, with a volume of 60 ml.

Fig. 1. Schematic diagram of hydrothermal and solvothermal experiments

3.2 Structural Characterization

3.2.1 X-ray Diffraction.

X-rays are electromagnetic waves with wavelengths ranging from 0.1 to 10 nm.

The material structure within crystals exhibits a high degree of order. When monochromatic X-rays penetrate a crystal, the electromagnetic fields of the subbands interact with the electron cloud. Since the electron cloud carries a negative charge, the electric field component of the X-rays drives the electron cloud into forced oscillations. Secondary waves emitted by different atoms interfere during spatial propagation. By recording the two-dimensional distribution patterns of diffraction spots using an X-ray diffractometer, these patterns can be converted into electron density distribution maps through inversion algorithms. This principle resembles using sound waves to reverse-engineer the location of a sound source, enabling the reconstruction of the three-dimensional arrangement of atoms within the crystal[5].

3.2.2. Transmission Electron Microscope.

With the help of the interaction between a high-energy electron beam and matter, a projection electron microscope can reconstruct microstructure information by collecting electron signals penetrating the sample. The electron beam will form a parallel beam with a diameter of 1-10 nm after being focused by a double condenser system. When high-energy electrons penetrate the ultra-thin sample chamber, Coulomb interaction will occur between electrons and nuclei, and this elastic scattering will form diffraction patterns, which can be used for crystal structure analysis. In addition, electrons also transfer some energy to the outer electrons of atoms. Different detectors can collect the electronic signals that penetrate the sample, thus forming a variety of imaging modes. For this, only unscattered or small-angle elastically scattered electrons can be collected to form an image with brightness related to sample thickness/atomic number. This imaging can be used to observe the internal defects of crystals and the distribution of nanoparticles. In addition, a specific diffraction beam can be selected for imaging by inserting an objective diaphragm to ensure that the microscope only displays the crystal grains meeting Bragg conditions. This dark imaging method can be used to analyze the orientation or phase distribution of crystals[6].

3.3 Electrochemical Test

3.3.1. Preparation of Batteries.

In the battery preparation process, this paper primarily employs the coating method to fabricate electrodes. Compared to traditional preparation methods, this approach enables precise control over the loading amount of active material. Accordingly, this study mixes the active material with a conductive agent and binder, and then coats the resulting slurry onto the substrate surface. Through drying and calendering operations, a porous electrode structure is formed on the surface. Acetylene black was employed as the primary conductive agent, with activated carbon selected as the secondary conductive enhancer. This choice stems from acetylene black's high specific surface area, enabling synergistic interaction with activated carbon to collectively reduce electrode surface

resistance. For the binder system, considering the chemical inertness and mechanical stability of polytetrafluoroethylene (PTFE), a heat-treated modified PTFE emulsion was adopted.

3.3.2. Cycling Voltammetry Test.

To investigate the electrochemical properties of substances, this study employs cyclic voltammetry to measure their redox potentials. For this experiment, a thermodynamically stable potential that does not induce side reactions on the electrode surface is selected as the starting point, and a unidirectional potential scan is conducted at a constant rate.

4 Synthesis and Characterization of $ZnFe_2O_4$ Nanomaterials

4.1 Synthesis of $ZnFe_2O_4$ Nanomaterials by Hydrothermal Method

Under ultrasonic conditions, we dissolve 1 mmol of $ZnCl_2$ and 2 mmol of $FeCl_3 \cdot 6H_2O$ in deionized water. Then, we add an NaOH solution to adjust the pH to 9. Subsequently, we transfer the suspension to a stainless-steel PTFE high-pressure sealed reactor (the fill factor is not specified in the original text, so it can be added as needed, for example: "with a fill factor of 80%" if a value is assumed for clarity). After sealing the reactor, we place it in a constant-temperature hot-air oven at 200°C for 24 hours. We allow it to cool naturally to room temperature before removing the reactor. Then, we centrifuge the reaction product, wash it three times with deionized water and anhydrous ethanol, and dry it in an 80°C vacuum oven for 12 hours to obtain the reddish-brown product. The obtained product is sintered for 3 hours at 500°C, 600°C, and 700°C in a muffle furnace, yielding $ZnFe_2O_4$ nanomaterials under different heat-treatment temperatures.

Figure 2 shows the XRD spectra of $ZnFe_2O_4$ samples obtained after heat treatment at 500°C, 600°C, and 700°C for the hydrothermal products synthesized at 200°C.

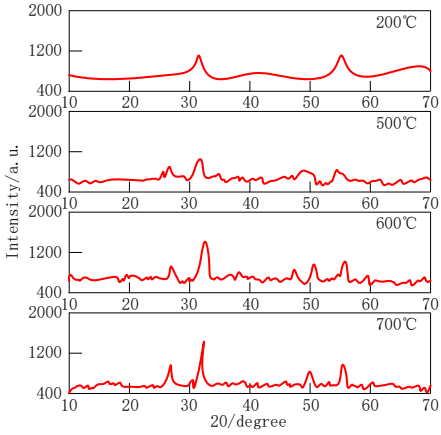

Fig. 2. XRD patterns of $ZnFe_2O_4$ samples obtained after heat treatment at 500°C, 600°C, and 700°C for the hydrothermal products at 200°C

From the figure, it can be seen that all the diffraction peaks in the XRD patterns of $ZnFe_2O_4$ samples obtained after heat treatment at 200°C, 500°C, 600°C, and 700°C can be attributed to $ZnFe_2O_4$ with an Fd3m crystal system (space group for spinel structure), which matches the standard card. No impurities were found, indicating a high purity of the product.

The figure also shows that as the heat-treatment temperature increases, the diffraction peaks of the $ZnFe_2O_4$ sample become sharper, with increasing peak intensity and decreasing half - peak width. This indicates that as the heat-treatment temperature rises, the disordered arrangement of atoms or ions in the sample becomes more ordered, the particle size increases, and the resulting $ZnFe_2O_4$ crystal form becomes increasingly perfect.

4.2 Characterization of $ZnFe_2O_4$ Nanomaterials

Figure 3 shows the TEM images of 200℃ samples prepared by the hydrothermal method and $ZnFe_2O_4$ samples obtained by heat treatment at 500℃, 600℃, and 700℃.

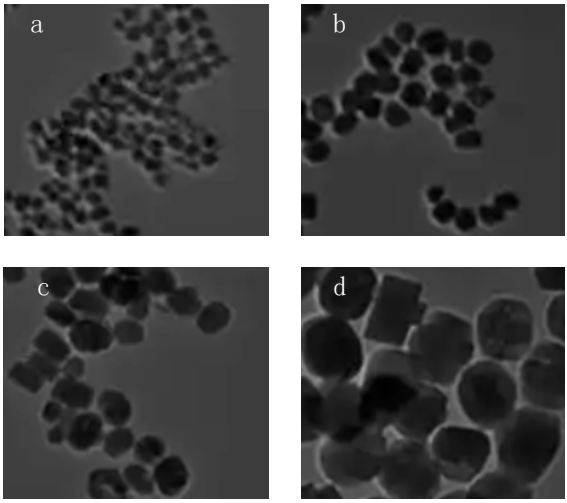

Fig. 3. TEM images of the samples obtained by the hydrothermal method at 200℃ and their $ZnFe_2O_4$ samples after heat treatment at 500℃, 600℃, and 700℃

From the figure, it can be seen that when the reaction temperature is 200℃, the product consists of nanoscale particles with good dispersion and uniform particle size distribution, with an average particle size of about 15 nm. In Figures 3 (b-d), it is observed that after thermal treatment, the particles aggregate, increasing their size. Moreover, as the temperature of thermal treatment increases, the particle size of the samples also gradually increases. When the temperature rises to 700℃, the aggregation of particles becomes more pronounced and severe, with some even increasing to 50 nm.

5 Synthesis and Characterization of 5 $ZnFe_2O_4$ Nanomaterials and Graphene Composites

5.1 Synthesis of $ZnFe_2O_4$/graphene composites

A certain amount of graphene nanosheets prepared by chemical exfoliation was added to 50 mL of ethylene glycol, and ultrasonication was used to form a uniformly dispersed solution. Then, 1 mmol $ZnCl_2$ and 2 mmol $FeCl_3 \cdot 6H_2O$ were dissolved in the above solution under ultrasonic conditions. Subsequently, 10 mmol urea was added, and the solution was subjected to ultrasonication for 30 min.

Next, the solution was transferred to a 60 mL stainless-steel PTFE high-pressure sealed reactor with a fill level of 80%. After sealing the reactor, it was placed in a constant-temperature hot-air supply chamber at 200°C for 24 h. Once it had naturally cooled to room temperature, the reactor was removed.

The reaction product was centrifuged and then washed three times with deionized water and anhydrous ethanol, respectively. After that, it was dried in an 80°C vacuum oven for 12 h, yielding a black product.

The obtained product was sintered at 500°C under argon protection in a tube furnace for 3 h, resulting in $ZnFe_2O_4$/graphene composites[7,8]. Using the same method, $ZnFe_2O_4$/graphene composites with graphene mass contents of 5 wt%, 10 wt%, and 15 wt% were also prepared.

5.2 Characterization of $ZnFe_2O_4$/Graphene Composites

Graphene is a two-dimensional carbon nanomaterial with a large specific surface area, unique mechanical properties, and excellent electrical conductivity. These characteristics can significantly improve the electrochemical performance of lithium-ion electrode materials, particularly oxide anode materials. These anode materials not only have low Li^+ and electron conductivity but also tend to agglomerate during charging and discharging processes.

Table 1 shows the average particle size of $ZnFe_2O_4$/graphene composites with graphene contents of 5 wt%, 10 wt%, and 15 wt%.

Table 1. The average particle size of $ZnFe_2O_4$/graphene composites calculated by the Scherrer formula

Crystal plane	(220)	(331)	(400)	(333)	(440)	Average particle size
Grain size/nm 5 wt%G	26.9	26.2	21.2	26.1	21.3	24.3
Grain size/nm 10 wt%G	25.0	21.2	25.9	27.3	26.4	25.2
Grain size/nm 15 wt%G	26.2	24.7	26.9	25.9	26.0	25.9

According to Table 1, when the graphene content is 5 wt%, 10 wt%, and 15 wt%, the average crystal particle size is 24.3, 25.2, and 25.9 nm, respectively, which shows that the average particle size increases slightly with the increase of graphene content.

Figure 4 shows the TEM image of $ZnFe_2O_4$/graphene composites.

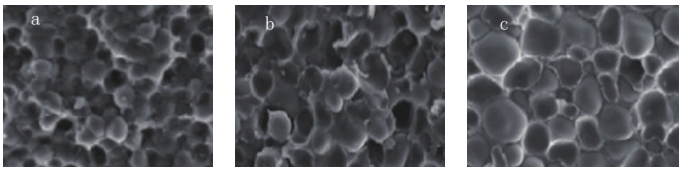

Fig. 4. TEM image of $ZnFe_2O_4$/graphene composites

Among them, "a," "b," and "c" represent $ZnFe_2O_4$/graphene composites with graphene contents of 5 wt%, 10 wt%, and 15 wt%, respectively. The figure illustrates that $ZnFe_2O_4$ nanospheres, with a particle size of 25 nm, are uniformly dispersed on the surface of graphene nanosheets. In Figure 4 (a), in addition to $ZnFe_2O_4$ nanospheres, there is also a small amount of nanoparticles attached to the graphene sheets. However, compared to the pure $ZnFe_2O_4$ samples prepared by solvothermal synthesis and subsequently heat-treated at 500°C, the amount of nanoparticles has decreased.

When the graphene content is 10 wt%, only $ZnFe_2O_4$ nanospheres are uniformly dispersed on the surface of graphene nanosheets, with no nanoparticles present. This may be because the increased graphene content reduces the presence of nanoparticles. When the graphene content is 15 wt%, only $ZnFe_2O_4$ nanospheres are uniformly dispersed on the surface of graphene nanosheets, but some nanospheres aggregate, with a few increasing in size to 500 nm. This indicates that as the graphene content increases, the number of nanoparticles decreases, promoting the formation of nanospheres. However, when the graphene content is too high, aggregation occurs, leading to an uneven distribution of nanosphere sizes.

Therefore, when the graphene content is 10 wt%, the $ZnFe_2O_4$/graphene composite exhibits the best morphological characteristics.

6 Conclusions

This paper not only analyzes the optimization of lithium-ion battery performance but also explores the design and application scenarios of nanocomposites. Considering the direct correlation between lithium-ion battery performance and electrode materials, nanocomposites were synthesized using the hydrothermal method. By continuously adjusting parameters such as temperature and reaction time during synthesis, flexible control over material composition and crystal structure was achieved. Experimental results demonstrate the advantages of nanocomposites in both charge/discharge rates and cycle life. Rational design of nanocomposite structures can effectively enhance the overall performance of lithium-ion batteries.

The above studies indicate the following:

(1) Porous spherical $ZnFe_2O_4$ nanomaterials, as anode materials for lithium-ion secondary batteries, show potential application prospects. Although the porous spherical $ZnFe_2O_4$ nano-electrode materials prepared by the solvothermal method exhibit high initial discharge capacity, their capacity fade is still relatively severe, and their cycle performance needs further improvement[9].

(2) Porous spherical $ZnFe_2O_4$/graphene composite electrode materials, as anode materials for secondary lithium-ion batteries, also show potential application prospects. This suggests the possibility of using such lithium-ion electrode materials in high-current discharge devices like electric vehicles or smart grids[10].

(3) Nanostructured composite materials also possess good thermal stability and safety, assuring the safe operation of lithium - ion batteries[4,6].

Use of AI

I used AI translation services to touch up the Results section. To improve the readability of this paper, I also used AI to help polish the statements in this research. After using these tools, I reviewed and edited the content as needed and take full responsibility for the content of the publication.

References

1. Deng Y., Hussain A., Raza W. Deng Y., Hussain A., Raza W., et al. Review on current development of polybenzimidazole membrane for lithium battery [J]. Journal of Energy Chemistry, 2024, 91 (4): 579-608. DOI: 10.1016/j.jechem.2023.12.044.
2. Duan T., Zhao L., and Wang L. D. X. Integrated Lithium Battery-Powered High-Field Asymmetric Ion Mobility Spectrometer (FAIMS) for Molecular Structure Fingerprinting and Deep Learning [J]. Analytical Letters, 2023, 56 (16/18): 2,836-2,850. DOI: 10.1080/00032719.2023.2185784.
3. Zhang Y., Kong W., and Zhang W. W. G. T. X. Comparative study on the performance of different thermal management for energy storage lithium battery [J]. Journal of Energy Storage, 2024, 85 (Apr.): 1.1-1.17. DOI: 10.1016/j.est.2024.111028.
4. Zargari F. and Nowroozi A. Thermophysical properties of choline chloride: 4ethylene glycol and $LiPF_6$ mixtures for lithium battery applications [J]. Ionics, 2025, 31 (2): 1,361-1,375. DOI: 10.1007/s11581-024-05962-y.
5. Cao H., Zhu G., Chen H., et al. Research on the impact of lithium battery ageing cycles on a data-driven lithium battery model [J]. World Wide Web, 2025, 28 (1): 1-23. DOI: 10.1007/s11280-024-01318-8.
6. He K., Wu J., Song J., He K., Wu J., Song J., et al. High-security organic PVDF-coated SiO_2 aerogel lithium battery separator [J]. Journal of Materials Science, 2024, 59 (43): 20,364-20,380. DOI: 10.1007/s10853-024-10360-w.
7. Tang M. B. X., et al. Dual-Cation CuAgSe-Based Material: Rapid Mass Transfer in Synthesis and High Thermoelectric Performance Realization [J]. ACS Applied Materials and Interfaces, 2024, 16 (17): 22,189-22,196. DOI: 10.1021/acsami.4c02217.
8. Suanto P., Saloma, and Nurjannah S. A. N. S. P. Synthesis of Nanocellulose as a Sustainable Construction Material from Waste Paper Using the Alkaline Method at Low Temperature [J]. Civil Engineering and Architecture, 2025, 13 (1): 175-192. DOI: 10.13189/cea.2025.130110.
9. Xu Z., Li J., Li L., et al. One-pot synthesis of ion-imprinted three-dimensional porous material based on graphene oxide for the selective adsorption of copper(II) [J]. Journal of Environmental Science and Health, Part A, 2023, 58 (6): 515-524. DOI: 10.1080/10934529.2023.2199650.

10. Kaikini A., George N. M., and Dalton P. V. R. Synthesis and characterization of Al-ion battery material as a potential substitute to Li-ion battery material [J]. Journal of advanced engineering research, 2024, 11 (1): 73-77. DOI: 10.1007/s10800-023-0195-3.